Delineation of Thermodynamic and Kinetic Factors that Control Stability in Non-fullerene Organic Solar Cells

Masoud Ghasemi,[1,2] Huawei Hu,[1,2] Zhengxing Peng,[1,2] Jeromy James Rech,[3] Indunil Angunawela,[1,2] Joshua H. Carpenter,[1,2] Samuel J. Stuard,[1,2] Andrew Wadsworth,[4] Iain McCulloch,[4,5] Wei You,[3] and Harald Ade[1,2,6,*]

SUMMARY

Although non-fullerene small molecular acceptors (NF-SMAs) are dominating current research in organic solar cells (OSCs), measurements of thermodynamics drivers and kinetic factors determining their morphological stability are lacking. Here, we delineate and measure such factors in crystallizable NF-SMA blends and discuss four model systems with respect to their meta-stability and degree of vitrification. We determine for the first time the amorphous-amorphous phase diagram in an NF-SMA system and show that its deep quench depth can result in severe burn-in degradation. We estimate the relative phase behavior of four other materials systems. Additionally, we derive room-temperature diffusion coefficients and conclude that the morphology needs to be stabilized by vitrification corresponding to diffusion constants below 10^{-22} cm^2/s. Our results show that to achieve stability via rational molecular design, the thermodynamics, glass transition temperature, diffusion properties, and related structure-function relations need to be more extensively studied and understood.

INTRODUCTION

The performance of solution-processed organic solar cells (OSCs) based on bulk heterojunction (BHJ) blends of a pair of donor and acceptor materials has greatly improved with the development of novel non-fullerene small molecular acceptors (NF-SMA).[1–5] With the power conversion efficiency (PCE) now reaching 12%–14% in many single-layer research devices,[6–14] the principles governing operational stability are becoming very important and need to be understood.[15–19] The lifetime of an OSC can be limited by various factors, such as exposure to humidity,[20] photo-oxidation of the BHJ layer,[21] and morphological instability due to diffusion or aggregation and, crystallization even at room temperature (RT).[22] Because of the dominance of fullerenes as acceptors for more than two decades,[23–26] it is not surprising that most stability investigations to date have been focusing on fullerene-based OSCs. Given the clear difference in the molecular structure and size of the non-fullerene and fullerene acceptors, the chemical and morphological stability of the NF-SMA OSCs cannot be extrapolated from data on fullerene devices. The stability of NF-SMA OSCs and, importantly, its thermodynamic drivers and mechanical or thermal factors that relate to vitrification, remain largely unexplored. To rationally enhance the operational lifetime of NF-SMA-based OSCs, the factors that control the morphological stability of the active layer need to be investigated and understood in depth.

Context & Scale

In recent years, the performance of organic solar cells (OSCs) has greatly improved with the development of novel non-fullerene small molecular acceptors (NF-SMA). The rapid increase in power conversion efficiency, now surpassing 15%, highlights an immediate and increasing need to understand the longevity and lifetime of NF-OSCs. However, the field relies mainly on a laborious trial-and-error approach to select polymer:NF-SMA pairs with desirable device stability. Here, we provide a structure-property relation that explains the morphological stability and burn-in degradation due to excessive demixing or crystallization. The framework presented in our study shows that a specific balance of interactions between polymer and NF-SMA can offer a short-term solution against excessive demixing. Long-term morphological stability that also suppresses crystallization can only be achieved by freezing in the initial quenched morphology through the use of polymers and/or NF-SMAs with low flexibility.

An efficiency loss in the first few hundred hours of the operation of an unstable OSC is generally referred to as "burn-in" and can be caused by various factors such as trap state formation,[27] photo-oxidation and oligomerization,[28] degradation of interlayers,[29] and over-purification of the mixed domains.[22] Among these factors, we focus on the impact of morphological instabilities and refer to the impact on device degradation simply as "burn-in" hereafter, mindful that other factors can in principle also cause burn-in. Burn-in driven by over-purification of mixed domains and/or crystallization have been extensively studied and linked to morphological instability in fullerene-based systems,[22,30–32] but these two main morphological instabilities have just started to be investigated for NF-SMA-based devices, primarily in a phenomenological manner without elucidating thermodynamics drivers and kinetic factors and their relation to molecular design.[33,34] In the BHJ solar cell, the actual morphology typically comprises multiple phases depending on the materials used.[35,36] For an amorphous polymer donor and with suppression of the crystallization of the small molecule acceptor (SMA), the phase diagram is asymmetric and there are only two domains: the acceptor-rich small molecule domain that is almost pure in sufficiently immiscible systems, and the donor rich, mixed amorphous domain.[37] In addition to these two domains, a semi-crystalline donor based device has an additional pure polymer crystalline domain. The crystallization of the SMA (fullerene or NF-SMA) is usually prevented in fresh devices by quenching the acceptor into an amorphous, vitrified state.[15] This two- or three-phase morphology must be carefully optimized to maximize the photon absorption, exciton separation, and charge transportation and extraction simultaneously. Such an optimization often creates mixed domains with an unstable composition (Figure 1).[22,38–40] For crystallizable SMAs, the meta-stable state of the amorphous domains is governed by the binodal composition, also referred to as the miscibility gap.[41] The thermodynamically favored (stable) state involves SMA crystals, a state described by the liquidus in the phase diagram. This state depletes the mixed domains of SMA relative to the binodal because of the extra chemical potential of the crystals. Please note that we will use the term binodal or miscibility gap and liquidus for simplicity even in cases where the liquid phases have vitrified to an amorphous glass below the glass transition temperature T_g, and the phase boundaries correspond to solid-solid transitions. The binodal or miscibility gap is governed by the miscibility limit of the donor or acceptor materials in the majority phase, which can be parameterized in favorable cases by the effective amorphous-amorphous Flory-Huggins (F-H) interaction parameter χ.[42,43] It has been shown recently that the temperature-dependent $\chi(T)$ is quantitatively related to the domain purity and fill factor (*FF*) in a number of systems.[37] A relatively high χ is needed for strong-enough phase separation and, thus, high device *FF*. However, an excessive repulsive molecular interaction between donor and acceptor materials can lead to over-purification of the mixed domains (i.e., with an SMA concentration below the percolation threshold), which would negatively affect device performance predominantly because of charge trapping and mono-molecular recombination.[37,40,44,45] Schematics of the possible scenarios of morphology evolution in an upper critical solution temperature (UCST) polymer: SMA blend with an amorphous donor and crystallizable SMA with a low and an optimal miscibility are illustrated in Figure 1. Severe burn-in degradation can be expected when the optimal morphology is quenched near the percolation threshold and is far from the miscibility gap, referred to as a "low-" or "hypo-miscibility" system (Figure 1A). On the other hand, a device with a miscibility gap close to the percolation threshold (Figure 1B) during the normal device operation conditions is referred to as "optimal miscibility" and is expected to exhibit a relatively stable morphology and thus lower or slower burn-in degradation. Hyper-miscibility systems typically yield low performance[37] and are not further considered. One example of a

[1]Department of Physics, North Carolina State University, Raleigh, NC 27695, USA

[2]Organic and Carbon Electronics Lab (ORaCEL), North Carolina State University, Raleigh, NC 27695, USA

[3]Department of Chemistry, University of North Carolina at Chapel Hill, Chapel Hill, NC 27599, USA

[4]Department of Chemistry, Imperial College London, London SW7 2AZ, UK

[5]King Abdullah University of Science and Technology (KAUST), KAUST Solar Center (KSC), Thuwal 23955-6900, Saudi Arabia

[6]Lead Contact

*Correspondence: harald_ade@ncsu.edu

https://doi.org/10.1016/j.joule.2019.03.020

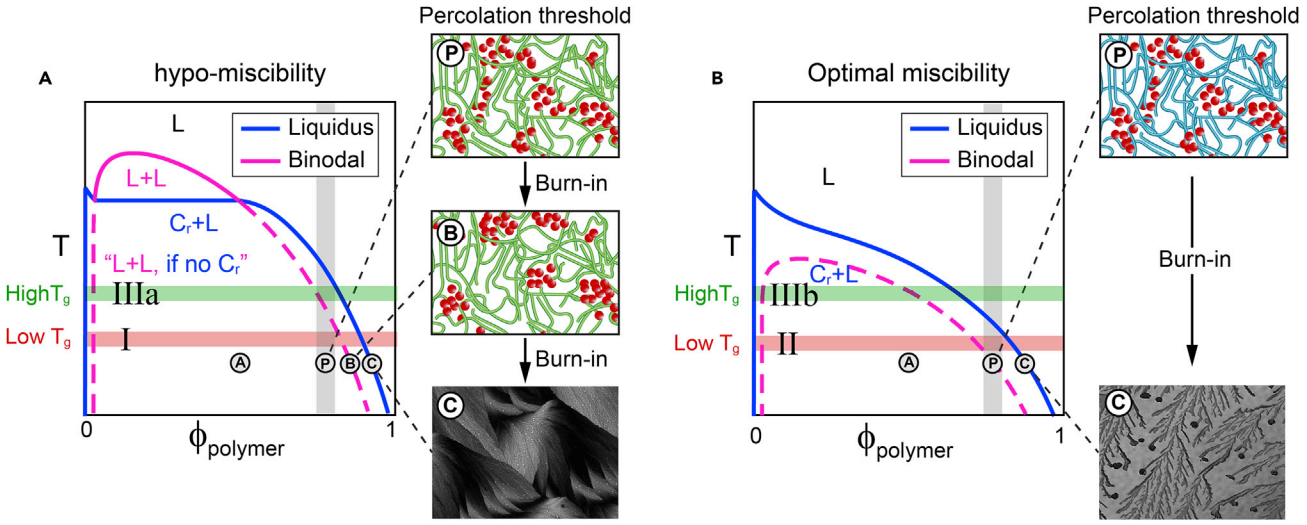

Figure 1. Motivational Illustrations of the Phase Diagrams and Schematic and Observed Morphologies of an Upper Critical Solution Temperature Polymer:NF-SMA Blend

(A) A blend with miscibility that is too low (hypo-miscible). Note that solid lines, including the blue part of the y axis, correspond to thermodynamic equilibrium, whereas dashed lines are only meta-stable states. Below T_g, which is composition and material dependent, the liquids are frozen into a glass. Equilibrium can still be established by diffusion but is kinetically hindered. The points A, P, and B represent initial average D/A ratio, percolation threshold of the SMA in the mixed domains, and the binodal composition at a given temperature, respectively. We note that the percolation threshold is ~25% of NF-SMA.[45] Point C represents the crystallization of NF-SMAs in a blend. The system generally proceeds from point A to point C during casting and aging, although initially, the presence of the solvent slightly alters the phase diagram. Processing conditions are typically chosen to reach the vicinity of point P, where an optimal trade-off between charge creation, charge extraction, and charge recombination is achieved if the domain size can be sufficiently controlled.

(B) A blend of an optimum amorphous-amorphous miscibility.

hypo-miscibility, high-performing polymer:SMA blend system (as illustrated in Figure 1A) is PffBT4T-2OD:$PC_{71}BM$, with a $PC_{71}BM$ meta-stable equilibrium concentration in the mixed domains well below the percolation threshold.[38,40] Consequently, abnormally strong burn-in degradation is observed in PffBT4T-2OD:$PC_{71}BM$ solar cells as [6,6]-phenyl C_{61} or C_{71} butyric acid methyl ester (PCBM) readily diffuses even at RT.[22] In contrast, PCDTBT:$PC_{71}BM$ is a near optimally miscible system, which should provide improved shelf stability with regard to demixing of the mixed domain when compared to PffBT4T-2OD:$PC_{71}BM$.[37] However, PCDTBT:$PC_{61}BM$ blends, similar to other fullerene-based OSCs, are prone to crystallization of the fullerene, and although these blends are thermodynamically stabilized against amorphous demixing, they are only kinetically stabilized against degradation by crystallization, the second main morphological degradation pathway.[46,47]

It is known that thermal annealing can boost the efficiency of many OSCs; however, heating may accelerate the transition of the morphology from the meta-stable miscibility gap to the liquidus or directly and simultaneously lead to crystallization failure as a result of nucleation or growth of SMA crystals.[15] The propensity for this transition to occur will depend on T_g, which is an indicator of the degree of vitrification at RT. Conceptually, there are three main classes of systems for crystallizable NF-SMA: class I systems that are unstable as a result of demixing and crystallization (low T_g case in Figure 1A), class II systems that have meta-stable mixed domains but can crystallize (low T_g case in Figure 1B), and class III systems that are kinetically stabilized irrespective of whether they are meta-stable or not (high T_g cases). Class III can be subdivided into class IIIa when a hypo-miscibility system is vitrified and class IIIb when an optimal miscibility, meta-stable system is vitrified.

In Figure 1, we measure the phase diagrams of NF-SMA OSC systems for the first time at least partially and delineate thermodynamic drivers and kinetic factors for stability in the three main classes of NF-SMA OSC systems delineated above. We select and utilize the well-known, prototypical NF-SMAs (i.e., EH-IDTBR and ITIC) selectively blended with the prototypical semiconductor polymers P3HT (semi-crystalline, ductile) and FTAZ (amorphous, ductile) to yield three different donor-acceptor blend-based systems in this study (P3HT:EH-IDTBR, FTAZ:EH-IDTBR, and FTAZ:ITIC) that systematically exemplify the characteristics of the different scenarios. We determine their device morphology and operational shelf-stability for variable processing conditions. We also investigate the thermodynamic drivers and kinetic factors of a previously reported relatively stable NF-SMA system based on another prototypical amorphous donor, namely PTB7-Th:EH-IDTBR,[19] as a comparison (the 4th system). It is found that P3HT:EH-IDTBR-based OSCs suffer from severe burn-in degradation in both as-cast and annealed samples. The severe efficiency loss of P3HT:EH-IDTBR devices is more pronounced in annealed devices compared to as-cast devices, even when these films are only briefly annealed at moderately elevated temperatures (120°C for 10 min). Even short periods of annealing are sufficient to nucleate crystals of the NF-SMA, which then assert their presence and negative influence over time. On the other hand, as-cast blend films based on FTAZ:EH-IDTBR exhibit low burn-in loss, whereas strong burn-in degradation occurs readily in annealed FTAZ:EH-IDTBR devices. In contrast, by substituting EH-IDTBR with ITIC, the FTAZ:ITIC-based systems provide OSCs with reduced burn-in degradation in both as-cast and low temperature annealed (120°C) devices, but with severe burn-in in high T annealed (180°C) devices. We determine $\chi(T)$ for P3HT:EH-IDTBR, the liquidus for FTAZ:EH-IDTBR, and FTAZ:ITIC-based systems, and the binodal at 110°C and 100°C for PTB7-Th:EH-IDTBR. In addition, we estimated RT diffusion coefficients of 1.7×10^{-17}, 2.0×10^{-18}, and 4×10^{-20} cm^2/s for EH-IDTBR in P3HT, FTAZ, and PTB7-Th, respectively, and analyzed device stability in light of the thermodynamic and kinetic knowledge gained. The diffusion coefficient of EH-IDTBR in P3HT- and FTAZ-based systems is sufficiently high to enable demixing and crystallization burn-in after low T annealing or even in as-cast devices. The more robust morphology of PTB7-Th:EH-IDTBR devices is attributed to the smaller diffusion coefficient of EH-IDTBR in PTB7-Th. These results indicate that NF-SMA OSCs can be stabilized by employing an NF-SMA with a high T_g or a polymer with lower ductility that suppresses the crystallization of the NF-SMA. In order for NF-SMA-based OSCs to be a viable technology, the quenched morphology that gives high performance has to be stabilized against demixing or crystallization by a high degree of vitrification with low diffusion ($\sim 1 \times 10^{-22}$ cm^2/s) or systems have to be meta-stable with a mixed composition near the percolation threshold, and the crystallization of the NF-SMA has to be suppressed or intrinsically avoided by novel molecular designs or blend formulation.

RESULTS

Devices

The photovoltaic properties of our NF-SMA-based devices are investigated in an inverted device architecture as depicted in Figure 2A. The chemical structures of the polymer donors (P3HT, FTAZ, and PTB7-Th) and NF-SMAs (EH-IDTBR, ITIC) used in this work are shown in Figure 2B. The typical current density-voltage (*J-V*) curves of the devices are presented in Figure 2C, and the averaged performance parameters for at least 6 OSC devices are summarized in Tables S1 and S2. Overall, the P3HT:EH-IDTBR solar cells achieved a PCE of 6.1%, which is comparable with the reported data.[48] The FTAZ:EH-IDTBR- and FTAZ:ITIC-based devices exhibit

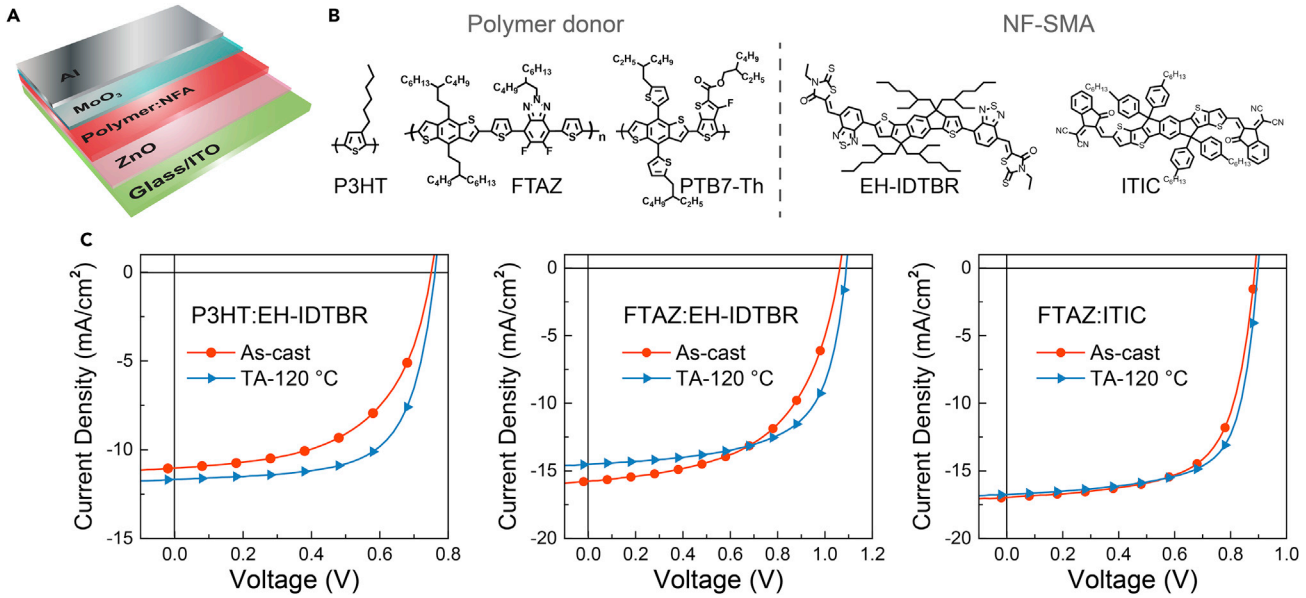

Figure 2. Chemical Structures and Photovoltaic Performance of Model Systems

(A) Device architecture of organic solar cells fabricated in this work.

(B) Chemical structures of P3HT, FTAZ, and PTB7-Th as electron donors and EH-IDTBR and ITIC as electron acceptors.

(C) Representative current density-voltage (*J-V*) characteristics of optimized fresh devices based on P3HT:EH-IDTBR, FTAZ:EH-IDTBR, and FTAZ:ITIC solar cells under 100 mW cm^{-2} simulated solar light. The thermally annealed samples were annealed at 120°C for 10 min. See also Table S1.

respectable efficiencies up to 10.2% and 10.6%, respectively. The devices employing FTAZ as the donor polymer give significantly improved performance compared to P3HT-based NF-SMA solar cells, which is likely because of enhanced hole mobility, better matched energy levels of the FTAZ polymer, and improved active layer morphology.[49,50]

Device Stability and Crystallization

Upon device fabrication, all devices were stored in the dark under N_2 atmosphere for device shelf-life stability tests and only periodically measured to minimize any possible impact of light and reveal just the morphology changes. Normalized PCE of the devices versus time are shown in Figure 3. Evolution of the key device parameters J_{SC}, V_{OC}, and *FF* as a function of time are shown in Figure S1. First, we compare the shelf-stability of the as-cast and annealed (120°C) devices of P3HT:EH-IDTBR, which exhibit an efficiency loss of 35% and 45% over 30 days, respectively (Figure 3A). In contrast, the as-cast FTAZ:EH-IDTBR-based solar cells decreased only 2% of its initial efficiency after 30 days but decreased over 30% after 30 days when thermally annealed for just 10 min at 120°C and subsequent dark storage at RT (Figure 3B). On the other hand, as-cast and low T thermally annealed (120°C) FTAZ:ITIC shows small burn-in degradation and only high T thermally annealing (180°C) produces degradation.

To reveal a possible proximal phenomenological origin of some of the efficiency loss observed, grazing incidence wide-angle X-ray scattering (GIWAXS) was used[51] to probe the impact of casting and thermal annealing on the nanoscale packing of the blend films. The corresponding 2D patterns of the investigated blend films are shown in Figures 3D–3I. 1D GIWAXS patterns of investigated blends are shown in Figure S2. From the GIWAXS profiles, the as-cast P3HT:EH-IDTBR (Figure 3D) blend

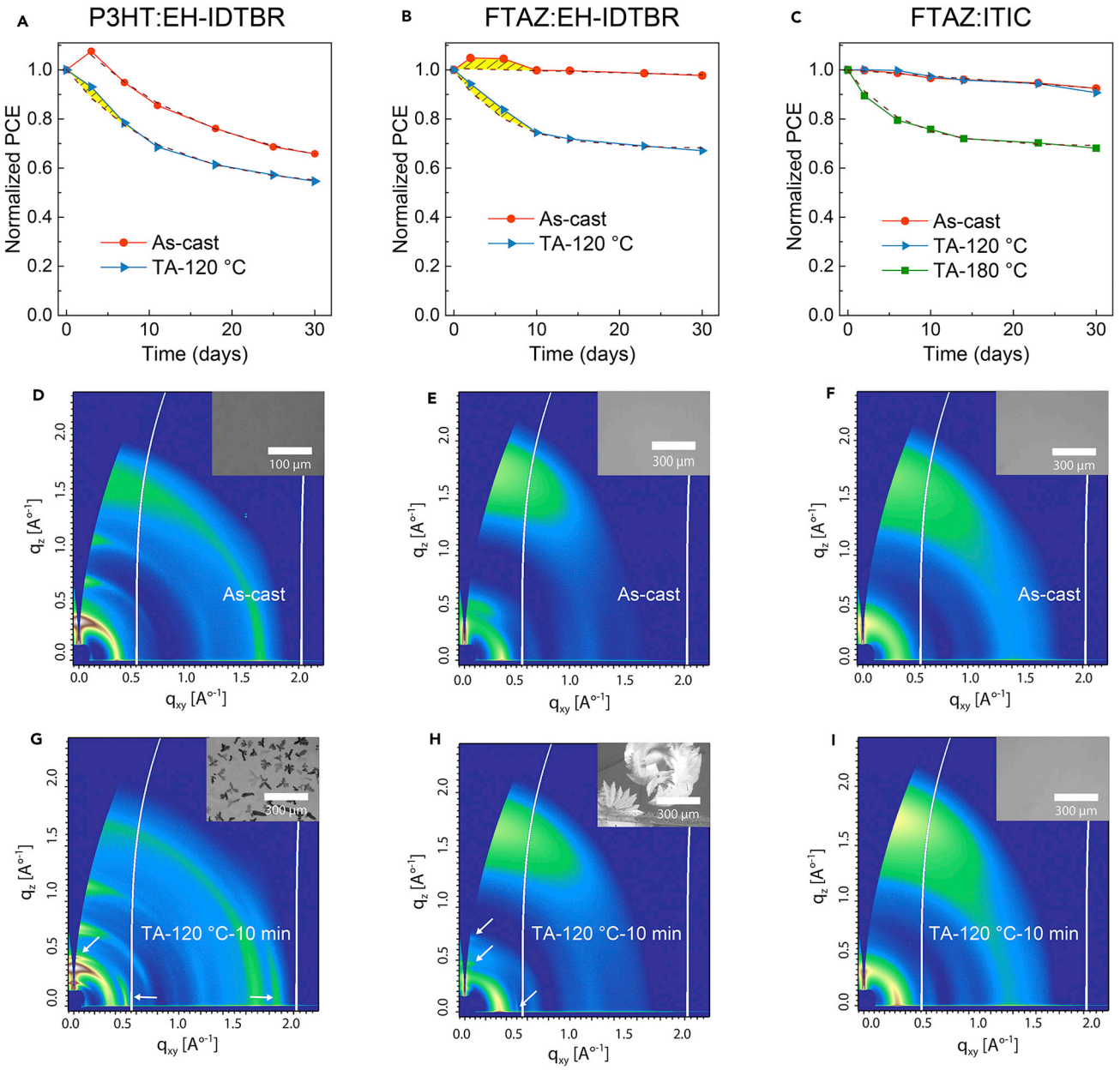

Figure 3. Shelf Stability and 2D GIWAXS Patterns

(A–C) Normalized PCE of NF-SMA based solar cells after 30 days storage in dark. Dashed lines represent fitted linear or exponential decays.

(A) P3HT:EH-IDTBR, (B) FTAZ:EH-IDTBR, (C) FTAZ:ITIC.

(D–F) 2D GIWAXS patterns of as-cast films of (D) P3HT:EH-IDTBR, (E) FTAZ:EH-IDTBR, and (F) FTAZ:ITIC samples. The yellow shaded area refers to deviations from the exponential decay fittings.

(G–I) 2D GIWAXS patterns of (G) P3HT:EH-IDTBR, (H) FTAZ:EH-IDTBR, and (I) FTAZ:ITIC samples annealed for 10 min at 120°C. The GIWAXS measurements were done 5 days after films' preparation. Insets are optical micrographs of the respective samples, except the samples were annealed for 24 h to enhance the growth of crystals so they can be observed by optical microscopy.

See also Tables S1 and S2 and Figures S1–S3.

film reveals a (010) peak in both the in-plane and out-of-plane directions, suggesting disordered texture. In addition, strong P3HT (100), (200), and (300) peaks are observed for this blend film, primarily in the out-of-plane direction. FTAZ:EH-IDTBR and FTAZ:ITIC (Figures 3E and 3F) blend films exhibit a well-defined and broad (010)

Table 1. Summary of the Stability and the Kinetic and Thermodynamic Properties of Materials and Blends

Blend	Annealing T (10 min)	T_{80} (Days)[a]	NF-SMA X-tals	Meta-stable	D (cm^2/s)	T_c (°C) NF-SMA	T_g (°C) Polymer[b]	Vitrified at RT	Class
P3HT:EH-IDTBR	n/a	15	no	no	1.7×10^{-17}	121	~20	no	I
P3HT:EH-IDTBR	120°C	7	yes	no	3.1×10^{-11}	121	~20	no	I
FTAZ:EH-IDTBR	n/a	190	no	~yes	2.0×10^{-18}	121	~20	no	II
FTAZ:EH-IDTBR	120°C	8	yes	~yes	3.0×10^{-12}[c]	121	~20	no	II
FTAZ:ITIC	n/a	75	no	~yes	n/a	200	~20	partial	IIIb
FTAZ:ITIC	120°C	65	no	~yes	n/a	200	~20	partial	IIIb
FTAZ:ITIC	180°C	6	yes	~yes	n/a	200	~20	partial	IIIb
PTB7-Th:EH-IDTBR	n/a	320	no	no	4×10^{-20}	121	125	~yes	IIIa
PTB7-Th:EH-IDTBR	120°C	206	no	no	1.6×10^{-14}	121	125	~yes	IIIa

[a]T_{80} of low burn-in devices such as as-cast FTAZ:ITIC was estimated by linear fit and extrapolation of the data. For PTB7-Th-EH-IDTBR devices last three points of normalized PCE versus time were used for linear fit and extrapolation.

[b]T_g of P3HT with 94 kDa molecular weight is calculated using the Flory-Fox equation presented by Gomez and coworkers. Also, T_g of FTAZ is inferred to be similar to P3HT because of the similar DSC results of the blends.[52]

[c]Estimated by assuming the activation energy is the same as that of EH-IDTBR into P3HT.

peak in the out-of-plane direction for both of the polymer donor and SMA and arc-like (100) scattering peaks, indicating the face-on preferential orientation of these materials. Most importantly, it is clear that there is essentially no observable feature representing crystals of EH-IDTBR and ITIC in as-cast samples. However, upon thermally annealing at 120°C for 10 min for the two EH-IDTBR-based blend films (i.e., P3HT:EH-IDTBR and FTAZ:EH-IDTBR, Figures 3G and 3H, respectively), clear crystal signature can be observed within these films, as the GIWAXS patterns exhibit multiple peaks of the NF-SMA of these blend films as indicated. Furthermore, optical microscopy images exhibit micrometer-sized crystals after thermal annealing at 120°C for EH-IDTBR-based blend films for 24 h (see insets in Figure 3), clearly supporting the conclusion that EH-IDTBR can crystallize readily at that temperature while blended with P3HT and FTAZ. In contrast, the GIWAXS pattern of FTAZ:ITIC annealed at 120°C (Figure 3I) does not show any small molecule crystalline features. Only the high-temperature annealing of FTAZ:ITIC (180°C, Figure S3) for 10 min leads to the formation of ITIC crystals and corresponding burn-in degradation.

Considering these results as summarized in Table 1, the three systems investigated fall clearly into three categories or classes of failure; (1) P3HT:EH-IDTBR failing severely even the as-cast devices presumably due likely to demixing and crystallization, (2) FTAZ:EH-IDTBR failing moderately only as a result of crystallization at low T anneal, and (3) FTAZ:ITIC only failing because of crystallization with aggressive annealing. For the remainder of our work, we investigate the underlying thermodynamic and kinetic factors of the working hypothesis that the severe failure of P3HT:EH-IDTBR can be retarded in the case of FTAZ:EH-IDTBR by eliminating the demixing of the mixed domains and progressively and more completely in case of FTAZ:ITIC by vitrifying the devices in accordance with the conceptual scenarios outlined above. The explanatory parameters investigated are meta-stability, diffusion coefficients, and thermal properties. These results are delineated in detail below and are also listed in Table 1.

Thermodynamic Properties: Toward Uncovering of Underlying Factors

To investigate the underlying origin of the differences of burn-in of the NF-SMA-based devices observed here and to be able to verify the framework as outlined in

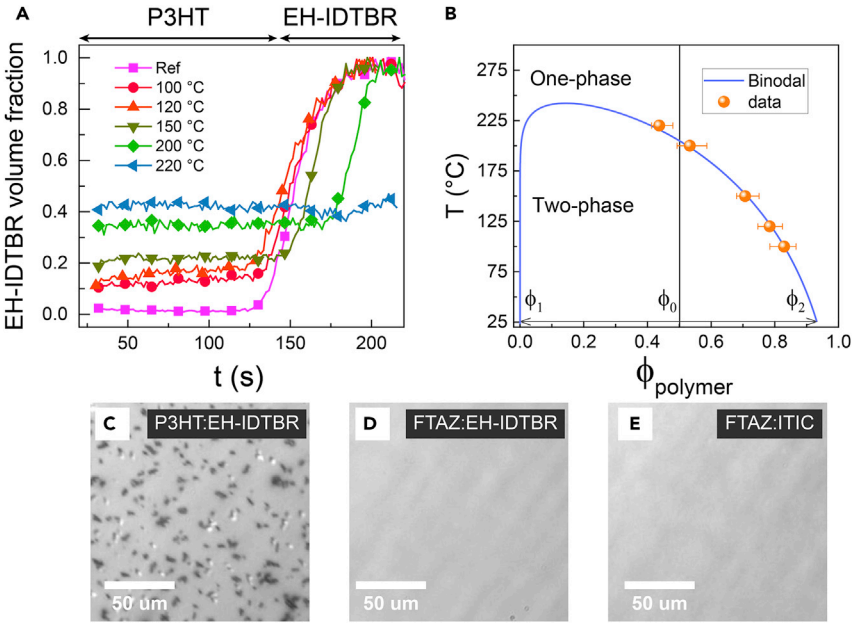

Figure 4. SIMS Profiles and Phase Diagram of P3HT:EH-IDTBR System

(A) Normalized SIMS profiles of P3HT/EH-IDTBR annealed at different temperatures.

(B) Corresponding miscibility gap/binodal extracted from temperature-dependent interaction parameter $\chi(T)$, after being normalized by the degree of crystallinity of P3HT (~25%). Error bars show the maximum and minimum volume fractions extracted from SIMS profiles at each temperature.

(C–E) VLM images of (C) P3HT:EH-IDTBR with 90:10 D/A, (D) FTAZ:EH-IDTBR with 85:15 D/A, and (E) FTAZ:ITIC with 85:15 D/A, after being thermally annealed at 160°C for 2 days, respectively. See also Figure S4.

Figure 1, we measured the molecular amorphous miscibility, which controls the phase separation and the limiting purity of the mixed domains in active layers.[22,40,37] We use a bilayer inter-diffusion experiment[53,54] (Figure 4A) and monitor with ToF-SIMS the equilibrium volume fraction of the EH-IDTBR in the polymer-rich layer under conditions where crystallization is sufficiently suppressed, thus mapping out the amorphous-amorphous phase diagram of the P3HT:EH-IDTBR system (see Supplemental Information and Figure S4 for details). By parameterizing the phase boundary within the F-H framework, the effective F-H amorphous-amorphous interaction parameter (χ) for P3HT:EH-IDTBR is derived to be $\chi(T) = -1.17 + 953/T$, where T is the absolute temperature. The good fit indicates that F-H is a reasonable approximation and reveals that P3HT:EH-IDTBR is a UCST system, for which increasing the temperature of the film will increase the degree of the mixing in the blend (Figure 4B). The fit yields an extrapolated χ = 2.03 at RT, which corresponds to a polymer-rich mixed phase with 7 vol % EH-IDTBR in the polymer, a concentration well below the percolation threshold of ~25%.[45]

Unfortunately, SIMS, as a method sensitive to molecular fragments, is not able to provide reliable inter-diffusion data for FTAZ:EH-IDTBR and FTAZ:ITIC as a result of the formation of similar molecular fragmentation patterns between FTAZ and these NF-SMAs. Consequently, we employed a recently introduced ultraviolet-visible (UV-vis) method to monitor the relative thermodynamic behavior of these blends.[55] The temperature-dependent miscibility in the presence of the NF-SMA crystals can be characterized by a combination of visible light microscopy and conventional UV-vis absorption spectroscopy.[55] Figure S5 shows the temperature

dependent UV-vis of the three systems used in this study. The presence of SMA crystals leads to higher purity in the mixed domains compared to the miscibility gap (see Figure 1).[56] Assuming that no cocrystals are formed, we have found (see Figure S6) that FTAZ:ITIC have mixed domains that are less pure than FTAZ:EH-IDTBR, which in turn are less pure than the P3HT:EH-IDTBR blend.

To confirm the validity of the relative thermodynamic behavior of these three different blends, we furthermore acquired visible light microscope (VLM) images of these systems annealed at elevated temperatures with a D/A ratio near the acceptor percolation threshold of the polymer:SMA blends. The P3HT:EH-IDTBR with 90:10 D/A ratio and FTAZ:NF-SMA blends with 85:15 D/A ratio were thermally annealed at 160°C for 2 days. VLM images show that there is no evidence of crystal features in FTAZ:EH-IDTBR- and FTAZ:ITIC-based blends, indicating that the equilibrium composition of the NF-SMA in the mixed phase of FTAZ:EH-IDTBR and FTAZ:ITIC is >15 vol % NF-SMA at the annealing temperature. In contrast, P3HT:EH-IDTBR blend film shows micron-sized crystals of EH-IDTBR even with a D/A ratio of 90:10, suggesting the equilibrium composition of EH-IDTBR in the mixed amorphous-amorphous phase is <10% EH-IDTBR, well below the acceptor percolation threshold.

Traversing the Threshold that Defines the Optimal Mixed-Domain Composition

The device stability data exhibit interesting details that warrant examination and might, in conjunction with our framework and characterization data, reveal nuanced information about the morphology evolution and underlying kinetic factors. Most strikingly, the PCE increases at the beginning for both as-cast EH-IDTBR-based solar cells (Figure 3). This is very likely because of the fact that the ideal morphology corresponding to the optimum percolation is located between the quenched morphology created during casting and the miscibility gap, which means that during the morphology evolution and demixing from the quenched morphology to the meta-stable miscibility gap, the performance likely goes first up because of reduced bimolecular recombination and then down because of trapping of charges and monomolecular recombination as percolation is lost. At the optimum trade-off between total recombination and energy per charge, the performance goes through the maximum. The concentration of NF-SMA in the mixed domains can be considered the optimum percolation for OPVs and must be a composition that is close to the percolation threshold for charge transport.

Interestingly, the annealed P3HT:EH-IDTBR and both FTAZ:EH-IDTBR systems also exhibit details in the stability data that we can relate to the crossing of the optimal composition of the mixed domains. To make this traversing of the optimum composition evident, we fit an exponential decay to the data (Figures 3A–3C). ITIC-based solar cells mainly evolve through a single exponential decay, most pronounced in FTAZ:ITIC device annealed at 180°C. In contrast, the two EH-IDTBR-based thermally annealed films and the as-cast FTAZ:EH-IDTBR do not decay with a clean exponential decay as observed in ITIC, but all three cases clearly have a second feature that can be described as an initial bump extending ~6 days for annealed P3HT:EH-IDTBR and ~10 days for both cases of FTAZ:EH-IDTBR. The timescale spanned by this feature is shorter in P3HT:EH-IDTBR than FTAZ:EH-IDTBR. The best exponential fit for as-cast P3HT:EH-IDTBR has been achieved when $t = 0$ is not included. The similarity of the data and the lack of other features in the device decay data suggest that only two variables, the demixing and crystallization, control this evolution.

Beyond Traversing the Optimum Composition Threshold: Secondary Impact of Demixing and Crystallization

Nuances of the detailed device stability data, particularly decreases observed in V_{OC} (see Figure S1), cannot be readily explained with local demixing of the mixed domains beyond the optimal composition, irrespective of whether such over purification is because of hypo-miscibility or crystallization. Other related secondary morphological factors and their evolution facilitated by diffusion and reorganization must be considered. Possible factors are the creation of a vertical stratification or wetting layer due to preferential interaction with and thus segregation to an interface, creation of large crystals that partially short the devices by penetrating the active layer completely, and molecular reorientation either at the electrodes or the D/A interfaces. Delineating which morphological factor precisely controls the degradation is outside the scope of this work. The secondary impacts are still predicated on the primary factors and their kinetics. To achieve some initial insight, we monitor the change in V_{OC} for P3HT:EH-IDTBR samples annealed at 80°C and 120°C at different timescales (Figure S7). As can be seen, annealing of EH-IDTBR-based systems consistently leads to loss of V_{OC}; the more severe the heat stress, the higher the resulting nucleation density and growth kinetics of crystals. Furthermore, to monitor the effect of crystallization on devices and accelerate the degradation process, we annealed the P3HT:EH-IDTBR devices at 150°C for 24 h after electrode deposition. The 150°C annealed devices show the largest V_{OC} loss (∼45%) with visible large EH-IDTBR crystals forming on the film. This trend clearly implies that it is the increased propensity to create crystals that leads to the V_{OC} loss. Even FTAZ:ITIC annealed at 180°C shows a V_{OC} loss. It is thus likely that a more substantial reorganization with crystals penetrating the whole film is the cause of the V_{OC} loss.

Diffusion Coefficients and Thermal Properties

The SIMS profiles of the P3HT:EH-IDTBR and the bump-feature in the device performance of P3HT:EH-IDTBR and FTAZ:EH-IDTBR also provides rough estimates for diffusion coefficients in these systems. The bumps in the device performance data provide a timescale that when combined with estimates of the size of the mixed domains from resonant soft X-ray scattering (R-SoXS), can be used to infer diffusion constants at RT. Estimating that domains have reached local equilibrium within ∼6 and ∼10 days for P3HT:EH-IDTBR and FTAZ:EH-IDTBR, respectively, and using domains spacing of 118 and 52 nm from R-SoXS (see Figure S8 for more information), respectively, we estimate diffusion constants D^{demix} at RT of 1.7×10^{-17} and 2.0×10^{-18} cm^2/s for P3HT:EH-IDTBR and FTAZ:EH-IDTBR, respectively. The following assumptions were made. Although the average domain size in BHJ blend will depend on the details of the morphology even for fixed volume fraction, a rough estimate of the maximum length over which diffusion has to occur to leave a domain in any directions corresponds to roughly half the spacing of the domains for a D/A volume fraction of ∼1/2. As a result, length scales of 59 and 26 nm were used to calculate the diffusion constants of P3HT:EH-IDTBR and FTAZ:EH-IDTBR, respectively. Furthermore, using the same diffusion length equation $x = 2(D \times t)^{0.5}$ where x, D, and t are diffused distance in cm, diffusion coefficient in cm^2/s, and annealing time in seconds, respectively; we calculate from SIMS a lower limit of the diffusion coefficient of $D^{mix} \geq 2.7 \times 10^{-12}$ cm^2/s at 100°C for EH-IDTBR diffusing into P3HT. Assuming the usual Arrhenius-type diffusion for EH-IDTBR and using the two diffusion constants of $D^{mix} \geq 2.7 \times 10^{-12}$ cm^2/s at 100°C and $D^{demix} = 1.7 \times 10^{-17}$ at RT, we can furthermore estimate the diffusion activation energy of EH-IDTBR into P3HT matrix to be ∼35 kcal/mol.[57] We should note that because of the possible differences between the mixing and demixing diffusion properties

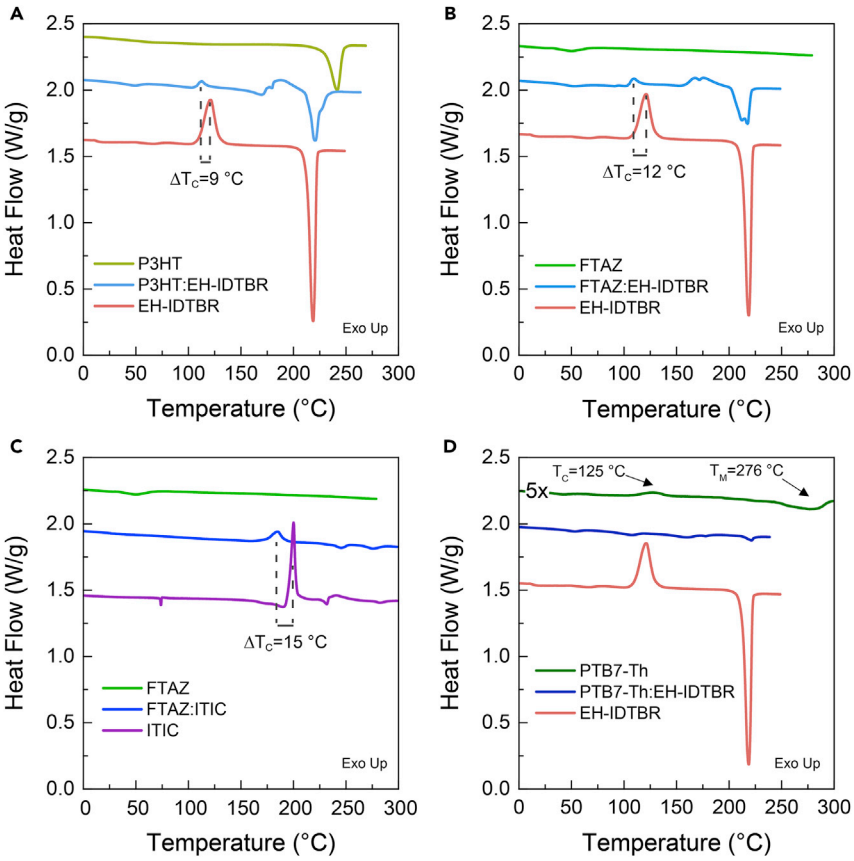

Figure 5. DSC Thermograms of Polymer:NF-SMA Blends

(A–D) DSC thermograms of (A) P3HT, P3HT:EH-IDTBR (1:1), and EH-IDTBR, (B) FTAZ, FTAZ:EH-IDTBR (1:1), and EH-IDTBR, (C) FTAZ, FTAZ:ITIC (1:1), and ITIC, and (D) PTB7-Th, PTB7-Th:EH-IDTBR (1:1), and EH-IDTBR collected from first heat cycle with 10°C/min heating rate. It is worth noting that, for the sake of comparison of the thermodynamic properties, the D/A ratios are kept at 1:1 for different blends. The thermograms were vertically shifted to improve visibility. To magnify the crystallization and melting transition features in PTB7-Th the data are multiplied by five.

of an SMA into or out of a polymer matrix in the presence or absence of SMA aggregate phases, the E_a calculated for P3HT:EH-IDTBR might not reflect the exact E_a that would be calculated when using solely a mixing or demixing dataset. Prior experiments of mixing versus demixing in P3HT:PCBM have not revealed though a large differences in D for these two scenarios.[58,59]

In order to elucidate the differences in temperature needed to readily cause crystallization and understand the differences in diffusion properties, the thermal proprieties of the neat polymers, NF-SMAs, and blends with device D/A ratios are examined by differential scanning calorimetry (DSC). From the DSC data (as shown in Figure 5), we can observe a cold crystallization peak at 121°C and 200°C for EH-IDTBR and ITIC, respectively, suggesting the initially amorphous fraction in the pure samples is reorganizing and crystallizing at these temperatures. We interpret the cold crystallization to reflect the T_g of the material fraction that is in an amorphous disordered state. T_g is difficult to observe unobstructed in the materials systems in this study because of the strong tendency of these materials to crystallize at a very similar temperature once the mobility increases at or near T_g. Furthermore, the cold crystallization temperatures of both EH-IDTBR and ITIC shift to slightly

lower temperatures upon mixing with P3HT or FTAZ, which is due to plasticization of the NF-SMA mixed with a ductile, low T_g polymer.[60] P3HT is known to be a ductile polymer with a T_g of ~20°C, which typically is a function of the polymer molecular weight.[52] The similar shift in cold crystallization temperature of 9°C and 12°C for EH-IDTBR in P3HT and FTAZ blends, respectively, suggests a similar ductility and T_g of these two polymers. We note that we were forced to observe the T_g indirectly, as no direct signature can be observed for T_g in DSC for P3HT or FTAZ. Overall, the DCS suggests that P3HT:EH-IDTBR and FTAZ:EH-IDTBR have similar diffusion properties. In contrast, the difference in T_g observed between the two NF-SMAs implies vastly different diffusion constants at a given temperature for the two NF-SMAs and thus a difference in vitrification.

Comparison to PTB7-Th:EH-IDTBR and Impact of Ductility and T_g of Donor Polymer

To extend the generality of our findings of three primary classes, we investigate the thermodynamic and kinetic factors of PTB7-Th:EH-IDTBR, a system that has recently been shown to have promising long-term device stability.[19] In order to understand the morphological stability of PTB7-Th:EH-IDTBR devices, we also test the shelf stability of these devices. PTB7-Th:EH-IDTBR devices provide promising shelf stability with a T_{80} of 320 and 206 days for as-cast and low temperature annealed (120°C), respectively (see Figure S9). In addition to the known and confirmed device performance of this system, we use the known mechanical and thermal properties of PTB7-Th to establish some structure-property relations.[19] By using the bilayer inter-diffusion method, we obtained diffusion profiles as shown in Figure 6A, which have been fitted with the 1D Fickian diffusion equation.[57,58] The quality of the fit indicates that the composition of the profiles at the interface, i.e., the fitting parameter C(0), is a good estimate of the binodal. The similar SMA composition at the interface ($C_{120}(0) \approx 38$ vol %) for PTB7-Th/EH-IDTBR bilayer samples after annealing at 120°C annealed for 3 and 10 min further confirms that SMA composition at the interface should be considered as the equilibrium composition (see Figure S10). Even without detailed parameterization of the phase behavior spanned by these three data points, qualitatively extrapolating the 120°C, 110°C, and 100°C data with equilibrium composition of 38, 29, and 15 vol % (see Figure 6A), respectively, to RT indicates that PTB7-Th:EH-IDTBR is not meta-stable, as the binodal is already below the percolation threshold at 100°C and should be declining further for lower T. In order to asses kinetics, the temperature-dependent diffusion coefficient *D(T)* was extracted from the SIMS profiles (Figure 6B) assuming Arrhenius type diffusion. Our *D(T)* results show that EH-IDTBR diffuses into the PTB7-Th matrix with two to three orders of magnitudes lower diffusion coefficient compared to diffusion into P3HT and FTAZ. Additionally, the DSC thermograms of PTB7-Th (see Figure 4D) shows small cold crystallization and melting peaks (T_m) at 125°C and 276°C, respectively. Given that T_c is a proxy for the T_g, this indicates that PTB7-Th has a significantly higher T_g than P3HT and FTAZ. The higher melting point of PTB7-Th compared to P3HT also points to higher T_g of PTB7-Th, using the T_g/T_m ratio rule.[61] The DSC thermogram of PTB7-Th:EH-IDTBR also shows the crystallization peak and subsequently melting peak suppression of EH-IDTBR compared to the blends of EH-IDTBR with P3HT and FTAZ. Furthermore, it was also shown by Balar and coworkers that PTB7-Th shows smaller ductility compared to P3HT,[62] which is consistent with the DSC results. We also acquired DSC data of EH-IDTBR blends with a 3:7 D/A ratio (see Figure S11). Similar to the 1:1 D/A ratio data, EH-IDTBR blended with FTAZ shows the largest drop in T_c, whereas EH-IDTBR blended with PTB7-Th does not experience a T_c drop. The higher T_g for PTB7-th leads to a more vitrified system with lower diffusion of EH-IDTBR into or out of the PTB7-Th

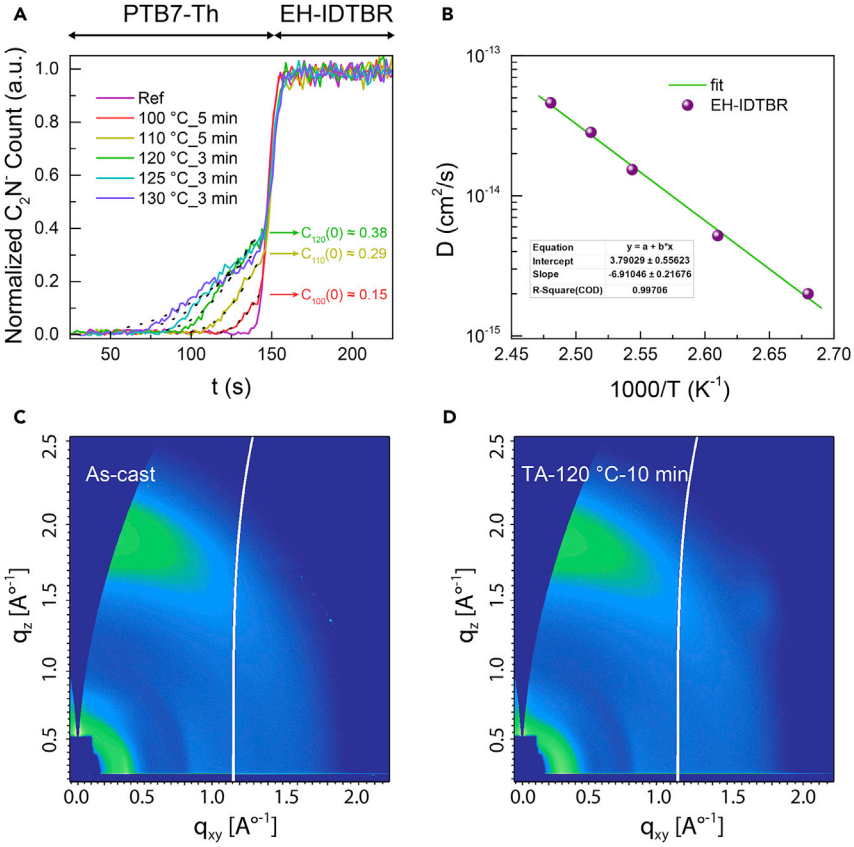

Figure 6. Temperature-Dependent Diffusion Coefficient *D(T)* and 2D GIWAXS Patterns

(A) Diffusion profiles of reference and annealed PTB7-Th/EH-IDTBR bilayers. The black dotted lines are the fits to diffusion profile using 1D Fick's second law solution for diffusion. Zero of the x axis represents the vacuum and polymer interface. The first 10–20 data points of the SIMS profiles were removed because of the instability of the sputtering and detecting beam in first 10–20 s. Assuming Arrhenius-type diffusion, activation energy E_a of 31.6 kcal/mol was extracted for diffusion of EH-IDTBR into PTB7-Th matrix. The profiles are horizontally shifted to align the polymer/SMA interface at 50% of EH-IDTBR yield.

(B) Temperature dependence diffusion coefficient of EH-IDTBR into PTB7-Th matrix.

(C and D) 2D GIWAXS patterns of (C) as-cast and (B) annealed (120°C for 10 min) PTB7-Th:EH-IDTBR blend films with 1:1.2 D/A ratio.

See also Figures S9 and S10.

matrix. The impact of lower ductility of PTB7-Th compared to P3HT and FTAZ is further explored using GIWAXS measurement. In contrast to the annealed P3HT:EH-IDTBR and FTAZ:EH-IDTBR systems, the as-cast (Figure 6C) and 120°C annealed (Figure 6D) PTB7-Th:EH-IDTBR films with 1:1.2 D/A ratio show no sign of EH-IDTBR crystalline features. Since the EH-IDTBR content in a 1:1.2 D/A blend is above the 38 vol % equilibrium composition of PTB7-Th:EH-IDTBR at 120°C, the lack of EH-IDTBR crystalline features in PTB7-Th:EH-IDTBR annealed samples is because of the vitrification of the morphology achieved by the lower ductility of PTB7-Th. The stability of the PTB7-Th:EH-IDTBR can be well explained by the low diffusion coefficient and the vitrification of EH-IDTBR in PTB7-Th. The combination of GIWAXS, DSC, and ToF-SIMS allow us to monitor and distinguish the effects of thermal annealing on a meta-stable system with relatively large diffusion coefficient (e.g., FTAZ:EH-IDTBR) from a hypo-miscible system with low diffusion coefficient (e.g., PTB7-Th:EH-IDTBR). For instance, in a meta-stable system with a relatively

large diffusion coefficient such as FTAZ:EH-IDTBR the annealing leads to nucleation and crystallization of EH-IDTBR. While in a hypo-miscible system with a relatively low diffusion coefficient such as PTB7-Th:EH-IDTBR, the crystallization is suppressed because of vitrification of the morphology.

A summary of the thermodynamic properties, the diffusion constants and thermal properties of all systems investigated are summarized in Table 1 to provide a comprehensive overview in one place of the device stability and the underlying materials' parameters.

DISCUSSION

In order to analyze and discuss commonalities and differences between our materials systems and relations to the three primary stability scenarios, we first summarize the most salient aspects of the materials systems, their relations to demixing and crystallization burn-in, then delineate commonalities, and return to structure-function relations and implications for the future.

Performance and Morphology Evolution and Their Classification

The P3HT:EH-IDTBR systems clearly corresponds to class I, exhibiting strong degradation due to crystallization and lack of meta-stability. The lack of meta-stability was directly confirmed by mapping out the phase diagram with SIMS and extracting $\chi(T)$. The extrapolated RT composition at the binodal was only 7 vol % EH-IDTBR, well below the percolation threshold. Additionally, rapid crystallization could be induced by mild annealing at 120°C for 10 min. The FTAZ:EH-IDTBR systems corresponds to Class II, exhibiting the highest T_{80} among the three primary model systems. Given that rapid crystallization and strong device performance degradation could be induced by mild annealing at 120°C for 10 min and that the estimated diffusion coefficient is not drastically different from that of P3HT:EH-IDTBR, we infer that this system is not kinetically stabilized and that the high T_{80} is due at least in part to FTAZ:EH-IDTBR being a system close to meta-stability. Various estimates of the phase behavior with optical methods have confirmed that FTAZ:EH-IDTBR should be closer to meta-stability than P3HT:EH-IDTBR.

The FTAZ:ITIC system is close to a class IIIb model system, exhibiting moderate T_{80} for as-cast devices and requiring high T annealing to induce crystallization. The system is clearly kinetically stabilized against crystallization and spinodal burn-in, although the direct confirmation by measuring a diffusion constant with SIMS was not possible. FTAZ:ITIC is the only system not showing an obvious initial increase or "bump." This implies that FTAZ:ITIC is not traversing the optimal composition near the percolation threshold within the experimental time frame.

PTB7-Th:EH-IDTBR is clearly close to a class IIIa model system, with a binodal EH-IDTBR concentration well below the percolation threshold and thus far from meta-stability but kinetically stabilized with the lowest diffusion constants observed.

Common Aspects of the Device Morphology and Degradation Kinetics

All observations about the device stability data and GIWAXS results can be consistently described with only three dominating variables: (1) the thermodynamic drivers for demixing or lack thereof (i.e., meta-stability) of the amorphous mixed regions, which is governing the evolution of the NF-SMA concentration from the as-cast, possibly quenched state toward the binodal, (2) the propensity of the NF-SMA to crystallize, which is governing the transition from the binodal to the liquidus, and (3) kinetic stabilization due to low diffusion. The overlapping characteristics of the

crystallization and demixing processes are clearly observed in the annealed devices of P3HT:EH-IDTBR and FTAZ:EH-IDTBR, when the impact of crystallization creates an exponential decay and the demixing a "bump" in the stability data. This clearly shows that burn-in because of crystallization is proceeding at the same time as the purification because of amorphous-amorphous interactions, possibly in different regions of the devices. Even the exponential function fitted to the as-cast P3HT:EH-IDTBR (Figure 3A) can be interpreted within this framework. The initial performance increase in as-cast devices is a result of demixing from an excessively quenched state to the optimum composition, whereas the exponential decay is dominated by delayed crystallization that happens even at RT after about 5 days. The definitive answer about the relative timing and weight of these two processes is outside the scope of the current study and would likely include analysis with higher data density in time and temperature and additional characterization methods. These results point out though that the evolution of the device performance has defined relations to the underlying thermodynamics of the system.

The observation of an initial increase in performance or a "bump" on top of a well-defined decay in three of the four systems investigated has interesting implications. First, it indicates that these devices have not been optimized with the currently used as-casting or post-processing procedures. Given this prevalence, this points possibly to competing fabrication constraints of locking in a small-enough length scale and the required quench to achieve small length scales is arresting the demixing of the mixed domains to a composition that is not optimal. Post-processing might be able to achieve improved performance by controlling the demixing to evolve toward the optimum composition. Such post-processing might require a judicious choice of temperature and might be constraint by the phase diagram. For example, annealing at elevated temperatures might allow the system to reach the binodal at that temperature. If that binodal corresponds to a mixed-domain composition that is too far above the percolation threshold, the quench back down to RT after the annealing step would lock-in this un-optimized composition. Consider, for argument's sake, an anneal of P3HT:EH-IDTBR at 200°C. It would produce a mixed-domain composition with 50% EH-IDTBR (Figure 3), which is much too high to give a good performance. There is thus a complex interrelation between processing, annealing protocols, and stability that depends on the details of the phase diagram. Second, a well-defined bump can be used in conjunction with measurements of the domains' size to estimate diffusion coefficients. In either case, the shape of the performance evolutions contains valuable information about the miscibility and the diffusion coefficients of the system. The observation of a bump would imply that there is sufficient mobility in the systems such that crystallizable NF-SMA might eventually crystallize and thus destroy the devices, although maybe with a delay similar to P3HT:EH-IDTBR. Additionally, deliberately creating mixed domains that are too impure and subsequently monitoring the bump in the device stability data might be an interesting method to infer diffusion coefficient in class I systems that could be performed in almost any laboratory, without needing SIMS or other complex measuring methods.

Kinetic Factors and Their Structure-Function Relations

The degree of vitrification and diffusion coefficients varies considerably between the systems. This must be ultimately related to molecular structure that controls interactions, flexibility, and thus various thermal and mechanical properties. Although our final goal is to directly understand structure-function relations at the molecular level, we have as a first step toward such understanding investigated proximal variables such as T_g and ductility. Overall, the difference and similarities in shelf-stability for

the two different NF-SMAs investigated and paired with FTAZ can be explained well by the differences in the T_gs and crystallization behavior of these two SMAs. Similarly, the ductility of the donor polymer could be linked to vitrification. Overall, the results indicate that use of a high-T_g, low-ductility polymer donor (e.g., PTB7-Th), or an SMA with a high T_g (e.g., ITIC) can suppress crystallization and demixing and leads to more stable operation. However, little is known about the mechanical and thermal properties for a number of donor polymers and NF-SMAs, even though such properties clearly impact the stability. For example, measuring T_g of semi-conducting polymers remains a challenge and which mechanical and thermal parameter controls stability and diffusion properties remains unresolved. We note that activation energy for diffusion of EH-IDTBR in P3HT is larger than that of PCBM in P3HT.[57] This is likely related to the shape and size of these two acceptor molecules.[63] This implies that the diffusion coefficient of NF-SMA of various shapes and possibly flexibility should be investigated as a function of both donor polymer and NF-SMA properties in order to more fully understand how devices can be vitrified and stabilized in relation to their chemical structure. These results also suggest that annealing protocols to boost efficiency have to be executed with caution in a system where the NF-SMA can crystallize. A temperature well below the T_g/cold crystallization temperature needs to be utilized to avoid the nucleation and crystallization of the NF-SMA.

For a hypo-optimal, low miscibility system, we estimate that a diffusion coefficient below 10^{-22} (cm^2/s) is required to provide sufficient kinetic stabilization. This corresponds to 20 nm diffusion over 10 years and is two orders of magnitude lower than what we observed for the most stable system here. Since P3HT:EH-IDTBR has a performance drop of 45% over 30 days because of a diffusion coefficient five orders of magnitude larger than what is required for a morphologically stable system and needs to have a quenched system for best performance, it is not an ideal system for industrial applications. We note that one of the PCBM-based systems with relatively good but not perfect morphological stability is PCDTBT:$PC_{71}BM$.[64] It is doubly stabilized with a binodal close to percolation[37] and relatively high vitrification because of a donor with T_g of ~140°C, which is much higher than that of P3HT.

Finally, the degradation of P3HT:EH-IDTBR is the highest among the three model systems. This is in contrast to a previously reported study by Gasparini and coworkers on an analog of EH-IDTBR, namely O-IDTBR with linear C8H17 side chains, in which "burn-in" free operation was reported for 300-nm-thick, blade-coated samples[34] but roughly in line with the thin, spin-cast P3HT:O-IDTBR devices reported by the same group that exhibited a drop in performance of ~25% over 50 days.[48] Clearly, processing conditions or film thickness seem to matter. The minor difference between the as-cast devices can have a number of causes, including differences in the P3HT batches used or different thermodynamic properties of the two IDTBR variants. Regarding the thermodynamics, DSC (Figure S12) reveals a larger depression of the melting and crystallization temperature of P3HT upon mixing with O-IDTBR compared to EH-IDTBR, suggesting a higher miscibility of P3HT:O-IDTBR compared to P3HT:EH-IDTBR. The thermodynamic driver for amorphous demixing would thus be smaller for P3HT:O-IDTBR and if small enough at RT to be a hyper-miscible or optimally miscible system, indeed burn-in free operation would be expected if crystallization is suppressed. Given that both IDTBR variants crystallize, the degradation of the spin-cast samples is likely because of crystallization induced by crystal nuclei formed during casting, which are not formed in blade-coating thicker films. The differences clearly warrants further study to better understand the differences

and if suppression of crystallization in blade-coated devices can persist in a real application environment with some thermal stress.

Conclusions

Considering the totality of the results, a coherent framework emerges that connects thermodynamics, kinetics, and fundamental thermal properties of the constituent materials. Our work is the first to experimentally demonstrate such comprehensive relationships, particularly in crystallizable NF-SMA systems. It confirms earlier inferences that low-miscibility NF-SMA systems have to be quenched for best performance[45] into a state that is thermodynamically unstable against demixing of the mixed domains. Furthermore, all systems investigated are intrinsically unstable against crystallization, which lowers the NF-SMA composition in the mixed domains further below the percolation threshold and can also lead to large crystals that short devices. Although conceptually simple, our work demonstrates explicitly that just three variables (demixing, crystallization, and diffusion) dominate the morphological stability for the systems investigated, and there is no indication that other factors such as molecular reorientation relative to the substrate or relative to the donor-acceptor interface or changes in charge transfer (CT) docking sites play a major role.[65–67] The impact of the demixing and crystallization variables can have similar timescales and can overlap in their impact. This is likely not accidental and meaningful diffusion and crystallization of the NF-SMA are likely systematically coupled (nonlinearly) via their T_g when starting from quenched morphologies. We have for the first time measured diffusion coefficients and outlined a new method to estimate at RT the diffusion coefficient for NF-SMA by using the device data and the morphology data. Comparisons to fullerene diffusion imply that NF-SMA are intrinsically more stable than fullerene devices, likely on account of differences in the shape of the acceptor.

The lessons learned from the combined measurements regarding a robust morphology are as follows: a system with optimal or hyper-optimal miscibility is intrinsically stable against demixing beyond the percolation threshold. If the crystallization can be controlled via entropic factors by using NF-SMA mixtures or by molecular design, an operationally stable system might be achieved. In all other cases, kinetic control of demixing and crystallization via vitrification is required. In those cases, the T_g of the NF-SMA and that of the donor polymer emerge as an important parameter predicting stability. Since T_g and ductility are likely anti-correlated, a stability-ductility tension emerges as an engineering challenge: the most stretchable and bendable devices are likely to be the most unstable. While that could have been conceptually anticipated, we show this here explicitly. The results point to a need for improved understanding of structure-function relations and the further development of measurement and analysis methods to achieve a rational design.

Importantly, our results refine and extend the prior findings that tuning of enthalpic molecular interactions is critical to achieving high performance.[37] It was argued that only systems with low-enough miscibility (i.e., high χ) can have strong-enough phase separation to yield high performance, in turn necessitating a quench of hypo-miscible systems into a highly non-equilibrium morphology.[38,40,37,45] We now relate the propensity for burn-in degradation of NF-SMA based OSCs not only directly to their measured molecular miscibility but also to the degree of vitrification of the polymer:NF-SMA blends and their diffusion properties. Importantly, we have shown that using a polymer with low ductility, such as PTB7-Th, and an NF-SMA with high T_g, such as ITIC, can lead to low diffusion coefficients, the vitrification of the OSC active layer, and suppression of NF-SMA crystallization. Given that ductility, glass formation, and diffusion properties are ultimately governed by complex molecular interactions, our results dictate that the inter- and intra-molecular interactions and possibly other

molecular parameters such as stiffness need to be tuned more precisely by molecular design than previously thought to either achieve optimum miscibility and thus at least meta-stability or to achieve sufficient vitrification. The results indicate that further extensive studies are warranted to delineate and control all molecular interactions and related structure-function relationships across several dimensions so that materials can be rationally designed for high performance and high stability.

EXPERIMENTAL PROCEDURES

Materials

P3HT is provided by Iain McCulloch's group with Mn ≈ 94 kDa and PDI = 1.6. FTAZ is provided by Wei You's group with Mn ≈ 57.5 kDa and PDI ≈ 1.6, which is synthesized according to previous literature.[68] PTB7-Th was purchased from Solarmer with Mn > 25 kDa and PDI between 1.8 and 2.2. EH-IDTBR and ITIC were purchased from 1-Material and Solamer, respectively. All the solvent and other materials were purchased from commercial sources and used without further purification.

Fabrication and Testing of Polymer:SMA Devices

The best performance for the polymer:SMA devices was achieved after extensive optimization with an inverted structure of ITO/ZnO/polymer:SMA/MoO_3/Al, and the details are as follows. Pre-patterned ITO-coated glass with a sheet resistance of ~15Ω per square was used as the substrate. It was cleaned by sequential sonication in soap deionized (DI) water, DI water, acetone, and isopropanol for 15 min at each step. After ultraviolet/ozone treatment for 20 min, a ZnO electron transport layer was prepared by spin coating at 4,000 rpm from a ZnO nanoparticle solution. Active layers were spin coated from the polymer:NF-SMA solution to obtain thicknesses of ~100 nm. P3HT:EH-IDTBR with 1:1 D/A active layers were spin cast from chlorobenzene (CB) solution with 12 mg/mL polymer concentration. FTAZ:NF-SMA active layers were cast from toluene solution with 6 mg/mL polymer concentration and 1:1.5 and 1:1 D/A ratio for FTAZ:EH-IDTBR and FTAZ:ITIC, respectively. PTB7-Th:EH-IDTBR active layers with 1:1.2 D/A ratio were cast from CB solution with 10 mg/mL polymer concentration. The thermally annealed polymer:NF-SMA films were then annealed at an elevated temperature for 10 min before being transferred to the vacuum chamber of a thermal evaporator inside the glove box. Then, a thin layer (10 nm) of MoO_3 was deposited as the anode interlayer under vacuum followed by 100 nm of Al as the top electrode. All cells were measured inside the glove box. For device characterizations, *J-V* characteristics were measured under AM1.5G light (100 $mWcm^{-2}$) using a Class AAA Newport solar simulator. The light intensity was calibrated using a standard Si diode (with KG5 filter, purchased from PV Measurement) to bring spectral mismatch to unity. *J-V* characteristics were recorded using a Keithley 236 source meter unit.

Hard and Soft X-Ray Scattering

GIWAXS[51] and R-SoXS[69] measurements were performed at the beamlines 7.3.3 and 11.0.1.2, Advanced Light Source (ALS), Lawrence Berkeley National Laboratory, as described in detail in the Supplemental Information.

Secondary Ion Mass Spectroscopy Measurements

For depth profiles acquired in this study, ToF-SIMS experiments were conducted using a TOF SIMS V (ION TOF, Inc. Chestnut Ridge, NY) instrument equipped with a Bi_3^+ liquid metal-ion gun, Cesium sputtering gun, and an electron flood gun for charge compensation. Cs^+ was used as the sputter source with a 10 keV energy and 24 nA current. The sputter area was 50 by 50 μm. The analysis chamber pressure was maintained below 5.0×10^{-9} mbar to avoid contamination of the surfaces to be

analyzed. The details of TOF-SIMS sample preparation are provided in the Supplemental Information.

DSC Measurements

The DSC samples were prepared by drop casting of the neat or blend materials dissolved in CB on glass slides with a total concentration of 15 mg/mL. After being stored inside the glovebox overnight, the samples were transferred into a vacuum chamber and kept under vacuum for 5 days to remove the residual solvent trapped in the film. The dried samples then were scratched from the glass slides and moved to aluminum pans to be used for DSC measurements. The DSC thermograms are collected with the TA Instruments Discovery DSC. The heating/cooling rate was 10°C/min. Baseline and temperature were calibrated with sapphire and indium.

SUPPLEMENTAL INFORMATION

Supplemental Information can be found online at https://doi.org/10.1016/j.joule.2019.03.020.

ACKNOWLEDGMENTS

NCSU gratefully acknowledges the support of ONR grant N000141712204 and KAUST's Center Partnership Fund (No. 3321). UNC supported by NSF grant (CBET-1639429). I.M. and A.W. acknowledge funding from EPSRC Project EP/M005143/1 and EC FP7 Project SC2 (610115). X-ray data were acquired at beamlines 11.0.1.2 and 7.3.3 at the Advanced Light Source, which is supported by the Director, Office of Science, Office of Basic Energy Sciences, of the U.S. Department of Energy under contract no. DE-AC02-05CH11231. SIMS was performed at the Analytical Instrumentation Facility (AIF) at NCSU, which is partially supported by the State of North Carolina and the National Science Foundation. The DSC instrument was purchased with UNC-GA ROI funds. C. Zhu, A. Hexemer, and C. Wang of the ALS (LBNL) provided instrument maintenance. Professor Enrique Gomez and Josh Litofsky are acknowledged for providing the initial FH program code. The authors acknowledge L. Ye for providing thoughtful and critical comments.

AUTHOR CONTRIBUTIONS

H.A. conceived the scientific framework with the help of M.G. M.G. designed experimental protocols, coordinated the experimental work, performed the SIMS/DSC measurements, and analyzed the SIMS/DSC data. M.G. made the GIWAXS and R-SoXS samples, and H.H. analyzed the GIWAXS and R-SoXS data. M.G. fabricated P3HT:EH-IDTBR, FTAZ:ITIC, and PTB7-Th:EH-IDTBR solar cell devices and performed the subsequent stability tests. H.H. fabricated and tested the FTAZ:EH-IDTBR devices. Z.P. performed and analyzed the temperature-dependent UV-vis data. M.G., H.H., and H.A. wrote the manuscript. J.J.R. and A.W. synthesized the FTAZ and P3HT polymers, respectively. H.H., I.A., J.H.C., and S.J.S. performed the GIWAXS and R-SoXS measurements. All authors provided comments on the manuscript and contributed to the editing. H.A. directed the study.

DECLARATION OF INTERESTS

The authors declare no competing interests.

Received: January 11, 2019
Revised: February 28, 2019
Accepted: March 18, 2019
Published: April 22, 2019

REFERENCES

1. Yan, C., Barlow, S., Wang, Z., Yan, H., Jen, A.K.-Y., Marder, S.R., and Zhan, X. (2018). Non-fullerene acceptors for organic solar cells. Nat. Rev. Mater. *3*, 18003.

2. Zhang, G., Zhao, J., Chow, P.C.Y., Jiang, K., Zhang, J., Zhu, Z., Zhang, J., Huang, F., and Yan, H. (2018). Nonfullerene acceptor molecules for bulk heterojunction organic solar cells. Chem. Rev. *118*, 3447–3507.

3. Li, S., Liu, W., Li, C.Z., Shi, M., and Chen, H. (2017). Efficient organic solar cells with non-fullerene acceptors. Small *13*, 1701120.

4. Nielsen, C.B., Holliday, S., Chen, H.Y., Cryer, S.J., and McCulloch, I. (2015). Non-fullerene electron acceptors for use in organic solar cells. Acc. Chem. Res. *48*, 2803–2812.

5. Lin, Y., Wang, J., Zhang, Z.G., Bai, H., Li, Y., Zhu, D., and Zhan, X. (2015). An electron acceptor challenging fullerenes for efficient polymer solar cells. Adv. Mater. *27*, 1170–1174.

6. Fei, Z., Eisner, F.D., Jiao, X., Azzouzi, M., Röhr, J.A., Han, Y., Shahid, M., Chesman, A.S.R., Easton, C.D., McNeill, C.R., et al. (2018). An alkylated indacenodithieno[3,2-b]thiophene-based nonfullerene acceptor with high crystallinity exhibiting single junction solar cell efficiencies greater than 13% with low voltage losses. Adv. Mater. *30*, 1705209.

7. Li, S., Ye, L., Zhao, W., Yan, H., Yang, B., Liu, D., Li, W., Ade, H., and Hou, J. (2018). A wide band gap polymer with a deep highest occupied molecular orbital level enables 14.2% efficiency in polymer solar cells. J. Am. Chem. Soc. *140*, 7159–7167.

8. Luo, Z., Bin, H., Liu, T., Zhang, Z.G., Yang, Y., Zhong, C., Qiu, B., Li, G., Gao, W., Xie, D., et al. (2018). Fine-tuning of molecular packing and energy level through methyl substitution enabling excellent small molecule acceptors for nonfullerene polymer solar cells with efficiency up to 12.54%. Adv. Mater. *30*, 1706124.

9. Li, T., Dai, S., Ke, Z., Yang, L., Wang, J., Yan, C., Ma, W., and Zhan, X. (2018). Fused tris(thienothiophene)-based electron acceptor with strong near-infrared absorption for high-performance as-cast solar cells. Adv. Mater. *30*, 1705969.

10. Sun, C., Pan, F., Bin, H., Zhang, J., Xue, L., Qiu, B., Wei, Z., Zhang, Z.G., and Li, Y. (2018). A low cost and high performance polymer donor material for polymer solar cells. Nat. Commun. *9*, 743.

11. Liu, W., Zhang, J., Zhou, Z., Zhang, D., Zhang, Y., Xu, S., and Zhu, X. (2018). Design of a new fused-ring electron acceptor with excellent compatibility to wide-bandgap polymer donors for high-performance organic photovoltaics. Adv. Mater. *30*, 1800403.

12. Xu, X., Yu, T., Bi, Z., Ma, W., Li, Y., and Peng, Q. (2017). Realizing over 13% efficiency in green-solvent-processed nonfullerene organic solar cells enabled by 1,3,4-thiadiazole-based wide-bandgap copolymers. Adv. Mater. *29*, 1703973.

13. Kan, B., Zhang, J., Liu, F., Wan, X., Li, C., Ke, X., Wang, Y., Feng, H., Zhang, Y., Long, G., et al. (2017). Fine-tuning the energy levels of a nonfullerene small-molecule acceptor to achieve a high short-circuit current and a power conversion efficiency over 12% in organic solar cells. Adv. Mater. *29*, 1704904.

14. Ye, L., Zhao, W., Li, S., Mukherjee, S., Carpenter, J.H., Awartani, O., Jiao, X., Hou, J., and Ade, H. (2016). High-efficiency nonfullerene organic solar cells: critical factors that affect complex multi-length scale morphology and device performance. Adv. Energy Mater. *6*, 1602000.

15. de Zerio, A.D., and Müller, C. (2018). Glass forming acceptor alloys for highly efficient and thermally stable ternary organic solar cells. Adv. Energy Mater. *8*, 1702741.

16. Baran, D., Ashraf, R.S., Hanifi, D.A., Abdelsamie, M., Gasparini, N., Röhr, J.A., Holliday, S., Wadsworth, A., Lockett, S., Neophytou, M., et al. (2017). Reducing the efficiency-stability-cost gap of organic photovoltaics with highly efficient and stable small molecule acceptor ternary solar cells. Nat. Mater. *16*, 363–369.

17. Cheng, P., and Zhan, X. (2016). Stability of organic solar cells: challenges and strategies. Chem. Soc. Rev. *45*, 2544–2582.

18. Jørgensen, M., Norrman, K., Gevorgyan, S.A., Tromholt, T., Andreasen, B., and Krebs, F.C. (2012). Stability of polymer solar cells. Adv. Mater. *24*, 580–612.

19. Baran, D., Gasparini, N., Wadsworth, A., Tan, C.H., Wehbe, N., Song, X., Hamid, Z., Zhang, W., Neophytou, M., Kirchartz, T., et al. (2018). Robust nonfullerene solar cells approaching unity external quantum efficiency enabled by suppression of geminate recombination. Nat. Commun. *9*, 2059.

20. Klumbies, H., Karl, M., Hermenau, M., Rösch, R., Seeland, M., Hoppe, H., Müller-Meskamp, L., and Leo, K. (2014). Water ingress into and climate dependent lifetime of organic photovoltaic cells investigated by calcium corrosion tests. Sol. Energy Mater. Sol. Cells *120*, 685–690.

21. Reese, M.O., Nardes, A.M., Rupert, B.L., Larsen, R.E., Olsen, D.C., Lloyd, M.T., Shaheen, S.E., Ginley, E.S., Rumbles, G., and Kopidakis, N. (2014). Photoinduced degradation of polymer and polymer–fullerene active layers: experiment and theory. Adv. Funct. Mater. *20*, 3476–3483.

22. Li, N., Perea, J.D., Kassar, T., Richter, M., Heumueller, T., Matt, G.J., Hou, Y., Güldal, N.S., Chen, H., Chen, S., et al. (2017). Abnormal strong burn-in degradation of highly efficient polymer solar cells caused by spinodal donor-acceptor demixing. Nat. Commun. *8*, 14541.

23. Yu, G., Gao, J., Hummelen, J.C., Wudl, F., and Heeger, A.J. (1995). Polymer photovoltaic cells - enhanced efficiencies via a network of internal donor-acceptor heterojunctions. Science *270*, 1789–1791.

24. Thompson, B.C., and Fréchet, J.M. (2008). Polymer-fullerene composite solar cells. Angew. Chem. Int. Ed. Engl. *47*, 58–77.

25. Dou, L., You, J., Hong, Z., Xu, Z., Li, G., Street, R.A., and Yang, Y. (2013). 25th anniversary article: a decade of organic/polymeric photovoltaic research. Adv. Mater. *25*, 6642–6671.

26. Hu, H., Chow, P.C.Y., Zhang, G., Ma, T., Liu, J., Yang, G., and Yan, H. (2017). Design of donor polymers with strong temperature-dependent aggregation property for efficient organic photovoltaics. Acc. Chem. Res. *50*, 2519–2528.

27. Peters, C.H., Sachs-Quintana, I.T., Mateker, W.R., Heumueller, T., Rivnay, J., Noriega, R., Beiley, Z.M., Hoke, E.T., Salleo, A., and McGehee, M.D. (2012). The mechanism of burn-in loss in a high efficiency polymer solar cell. Adv. Mater. *24*, 663–668.

28. Burlingame, Q., Tong, X., Hankett, J., Slootsky, M., Chen, Z., and Forrest, S.R. (2015). Photochemical origins of burn-in degradation in small molecular weight organic photovoltaic cells. Energy Environ. Sci. *8*, 1005–1010.

29. Kam, Z., Wang, X., Zhang, J., and Wu, J. (2015). Elimination of burn-in open-circuit voltage degradation by ZnO surface modification in organic solar cells. ACS Appl. Mater. Interfaces *7*, 1608–1615.

30. Mendaza, A.D., Melianas, A., Rossbauer, S., Bäcke, O., Nordstierna, L., Erhart, P., Olsson, E., Anthopoulos, T.D., Inganäs, O., and Müller, C. (2015). High-entropy mixtures of pristine fullerenes for solution-processed transistors and solar cells. Adv. Mater. *27*, 7325–7331.

31. Lindqvist, C., Bergqvist, J., Bäcke, O., Gustafsson, S., Wang, E., Olsson, E., Inganäs, O., Andersson, M.R., and Müller, C. (2014). Fullerene mixtures enhance the thermal stability of a non-crystalline polymer solar cell blend. Appl. Phys. Lett. *104*, 153301.

32. Schroeder, B.C., Li, Z., Brady, M.A., Faria, G.C., Ashraf, R.S., Takacs, C.J., Cowart, J.S., Duong, D.T., Chiu, K.H., Tan, C.H., et al. (2014). Enhancing fullerene-based solar cell lifetimes by addition of a fullerene dumbbell. Angew. Chem. Int. Ed. Engl. *53*, 12870–12875.

33. Cha, H., Wu, J., Wadsworth, A., Nagitta, J., Limbu, S., Pont, S., Li, Z., Searle, J., Wyatt, M.F., Baran, D., et al. (2017). An efficient, "burn in" free organic solar cell employing a nonfullerene electron acceptor. Adv. Mater. *29*, 1701156.

34. Gasparini, N., Salvador, M., Strohm, S., Heumueller, T., Levchuk, I., Wadsworth, A., Bannock, J.H., de Mello, J.C., Egelhaaf, H.-J., Baran, D., et al. (2017). Burn-in free nonfullerene-based organic solar cells. Adv. Energy Mater. *7*, 1700770.

35. Sweetnam, S., Graham, K.R., Ngongang Ndjawa, G.O., Heumüller, T., Bartelt, J.A., Burke, T.M., Li, W., You, W., Amassian, A., and McGehee, M.D. (2014). Characterization of the polymer energy landscape in polymer: fullerene bulk heterojunctions with pure and mixed phases. J. Am. Chem. Soc. *136*, 14078–14088.

36. Buchaca-Domingo, E., Ferguson, A.J., Jamieson, F.C., McCarthy-Ward, T., Shoaee, S., Tumbleston, J.R., Reid, O.G., Yu, L., Madec, M.-B., Pfannmöller, M., et al. (2014). Additive-assisted supramolecular manipulation of polymer: fullerene blend phase morphologies

and its influence on photophysical processes. Mater. Horiz. *1*, 270–279.

37. Ye, L., Hu, H., Ghasemi, M., Wang, T., Collins, B.A., Kim, J.H., Jiang, K., Carpenter, J.H., Li, H., Li, Z., et al. (2018). Quantitative relations between interaction parameter, miscibility and function in organic solar cells. Nat. Mater. *17*, 253–260.

38. Liu, Y., Zhao, J., Li, Z., Mu, C., Ma, W., Hu, H., Jiang, K., Lin, H., Ade, H., and Yan, H. (2014). Aggregation and morphology control enables multiple cases of high-efficiency polymer solar cells. Nat. Commun. *5*, 5293.

39. Müller, C. (2015). On the glass transition of polymer semiconductors and its impact on polymer solar cell stability. Chem. Mater. *27*, 2740–2754.

40. Ye, L., Collins, B.A., Jiao, X., Zhao, J., Yan, H., and Ade, H. (2018). Miscibility-function relations in organic solar cells: significance of optimal miscibility in relation to percolation. Adv. Energy Mater. *8*, 1703058.

41. Rathi, P., Huang, T.M., Dayal, P., and Kyu, T. (2008). Crystalline−amorphous interaction in relation to the phase diagrams of binary polymer blends containing a crystalline constituent. J. Phys. Chem. B *112*, 6460–6466.

42. Kouijzer, S., Michels, J.J., van den Berg, M., Gevaerts, V.S., Turbiez, M., Wienk, M.M., and Janssen, R.A.J. (2013). Predicting morphologies of solution processed polymer: fullerene blends. J. Am. Chem. Soc. *135*, 12057–12067.

43. Kozub, D.R., Vakhshouri, K., Orme, L.M., Wang, C., Hexemer, A., and Gomez, E.D. (2011). Polymer crystallization of partially miscible polythiophene/fullerene mixtures controls morphology. Macromolecules *44*, 5722–5726.

44. Bartelt, J.A., Beiley, Z.M., Hoke, E.T., Mateker, W.R., Douglas, J.D., Collins, B.A., Tumbleston, J.R., Graham, K.R., Amassian, A., Ade, H., et al. (2013). The importance of fullerene percolation in the mixed regions of polymer-fullerene bulk heterojunction solar cells. Adv. Energy Mater. *3*, 364–374.

45. Ye, L., Li, S., Liu, X., Zhang, X., Ghasemi, M., Xiong, Y., Hou, J., and Ade, H. (2018). Quenching to the percolation threshold in organic solar cells. Joule *3*, 443–458.

46. Li, Z., Ho Chiu, K., Shahid Ashraf, R., Fearn, S., Dattani, R., Cheng Wong, H., Tan, C.H., Wu, J., Cabral, J.T., and Durrant, J.R. (2015). Toward improved lifetimes of organic solar cells under thermal stress: substrate-dependent morphological stability of PCDTBT: PCBM films and devices. Sci. Rep. *5*, 15149.

47. Wong, H.C., Li, Z., Tan, C.H., Zhong, H., Huang, Z., Bronstein, H., McCulloch, I., Cabral, J.T., and Durrant, J.R. (2014). Morphological stability and performance of polymer–fullerene solar cells under thermal stress: the impact of photoinduced PC60BM oligomerization. ACS Nano *8*, 1297–1308.

48. Holliday, S., Ashraf, R.S., Wadsworth, A., Baran, D., Yousaf, S.A., Nielsen, C.B., Tan, C.H., Dimitrov, S.D., Shang, Z., Gasparini, N., et al. (2016). High-efficiency and air-stable P3HT-based polymer solar cells with a new non-fullerene acceptor. Nat. Commun. *7*, 11585.

49. Li, W., Albrecht, S., Yang, L., Roland, S., Tumbleston, J.R., McAfee, T., Yan, L., Kelly, M.A., Ade, H., Neher, D., et al. (2014). Mobility-controlled performance of thick solar cells based on fluorinated copolymers. J. Am. Chem. Soc. *136*, 15566–15576.

50. Dai, S., Zhao, F., Zhang, Q., Lau, T.K., Li, T., Liu, K., Ling, Q., Wang, C., Lu, X., You, W., et al. (2017). Fused nonacyclic electron acceptors for efficient polymer solar cells. J. Am. Chem. Soc. *139*, 1336–1343.

51. Hexemer, A., Bras, W., Glossinger, J., Schaible, E., Gann, E., Kirian, R., MacDowell, A., Church, M., Rude, B., and Padmore, H. (2010). A SAXS/WAXS/GISAXS beamline with multilayer monochromator. J. Phys. Conf. Ser. *247*, 012007.

52. Xie, R., Lee, Y., Aplan, M.P., Caggiano, N.J., Müller, C., Colby, R.H., and Gomez, E.D. (2017). Glass transition temperature of conjugated polymers by oscillatory shear rheometry. Macromolecules *50*, 5146–5154.

53. Treat, N.D., Varotto, A., Takacs, C.J., Batara, N., Al-Hashimi, M., Heeney, M.J., Heeger, A.J., Wudl, F., Hawker, C.J., and Chabinyc, M.L. (2012). Polymer-fullerene miscibility: a metric for screening new materials for high-performance organic solar cells. J. Am. Chem. Soc. *134*, 15869–15879.

54. Ro, H.W., Akgun, B., O'Connor, B.T., Hammond, M., Kline, R.J., Snyder, C.R., Satija, S.K., Ayzner, A.L., Toney, M.F., Soles, C.L., et al. (2012). Poly(3-hexylthiophene) and [6,6]-phenyl-C61-butyric acid methyl ester mixing in organic solar cells. Macromolecules *45*, 6587–6599.

55. Peng, Z., Jiao, X., Ye, L., Li, S., Rech, J.J., You, W., Hou, J., and Ade, H. (2018). Measuring temperature-dependent miscibility for polymer solar cell blends: an easily accessible optical method reveals complex behavior. Chem. Mater. *30*, 3943–3951.

56. Lindqvist, C., Sanz-Velasco, A., Wang, E., Bäcke, O., Gustafsson, S., Olsson, E., Andersson, M.R., and Müller, C. (2013). Nucleation-limited fullerene crystallisation in a polymer–fullerene bulk-heterojunction blend. J. Mater. Chem. A *1*, 7174.

57. Treat, N.D., Mates, T.E., Hawker, C.J., Kramer, E.J., and Chabinyc, M.L. (2013). Temperature dependence of the diffusion coefficient of PCBM in poly(3-hexylthiophene). Macromolecules *46*, 1002–1007.

58. Watts, B., Belcher, W.J., Thomsen, L., Ade, H., and Dastoor, P.C. (2009). A quantitative study of PCBM diffusion during annealing of P3HT: PCBM blend films. Macromolecules *42*, 8392–8397.

59. Treat, N.D., Brady, M.A., Smith, G., Toney, M.F., Kramer, E.J., Hawker, C.J., and Chabinyc, M.L. (2011). Interdiffusion of PCBM and P3HT reveals miscibility in a photovoltaically active blend. Adv. Energy Mater. *1*, 82–89.

60. O'Connor, B., Kline, R.J., Conrad, B.R., Richter, L.J., Gundlach, D., Toney, M.F., and DeLongchamp, D.M. (2011). Anisotropic structure and charge transport in highly strain-aligned regioregular poly(3-hexylthiophene). Adv. Funct. Mater. *21*, 3697–3705.

61. Young, R.J., and Lovell, P.A. (2011). Introduction to Polymers, Third Edition (CRC Press).

62. Balar, N., and O'Connor, B.T. (2017). Correlating crack onset strain and cohesive fracture energy in polymer semiconductor films. Macromolecules *50*, 8611–8618.

63. Deppe, D.D., Miller, R.D., and Torkelson, J.M. (1996). Small molecule diffusion in a rubbery polymer near Tg: effects of probe size, shape, and flexibility. J. Polym. Sci. B Polym. Phys. *34*, 2987–2997.

64. Peters, C.H., Sachs-Quintana, I.T., Kastrop, J.P., Beaupré, S., Leclerc, M., and McGehee, M.D. (2011). High efficiency polymer solar cells with long operating lifetimes. Adv. Energy Mater. *1*, 491–494.

65. Tumbleston, J.R., Collins, B.A., Yang, L., Stuart, A.C., Gann, E., Ma, W., You, W., and Ade, H. (2014). The influence of molecular orientation on organic bulk heterojunction solar cells. Nat. Photon. *8*, 385–391.

66. Collins, B.A., Cochran, J.E., Yan, H., Gann, E., Hub, C., Fink, R., Wang, C., Schuettfort, T., McNeill, C.R., Chabinyc, M.L., et al. (2012). Polarized X-ray scattering reveals non-crystalline orientational ordering in organic films. Nat. Mater. *11*, 536–543.

67. Jiao, X., Ye, L., and Ade, H. (2017). Quantitative morphology-performance correlations in organic solar cells: insights from soft X-ray scattering. Adv. Energy Mater. *7*, 1700084.

68. Zhang, Q., Yan, L., Jiao, X., Peng, Z., Liu, S., Rech, J.J., Klump, E., Ade, H., So, F., and You, W. (2017). Fluorinated thiophene units improve photovoltaic device performance of donor–acceptor copolymers. Chem. Mater. *29*, 5990–6002.

69. Gann, E., Young, A.T., Collins, B.A., Yan, H., Nasiatka, J., Padmore, H.A., Ade, H., Hexemer, A., and Wang, C. (2012). Soft x-ray scattering facility at the advanced light source with real-time data processing and analysis. Rev. Sci. Instrum. *83*, 045110.